

New physics in $b \rightarrow se^+e^-$: A model independent analysis

Ashutosh Kumar Alok,^{1,*} Suman Kumbhakar,^{2,†} Jyoti Saini,^{1,‡} and S Uma Sankar^{3,§}

¹*Indian Institute of Technology Jodhpur, Jodhpur 342037, India*

²*Centre for High Energy Physics, Indian Institute of Science, Bangalore 560012, India*

³*Indian Institute of Technology Bombay, Mumbai 400076, India*

The lepton universality violating flavor ratios R_K/R_{K^*} indicate new physics either in $b \rightarrow s\mu^+\mu^-$ or in $b \rightarrow se^+e^-$ or in both. If the new physics is only $b \rightarrow se^+e^-$ transition, the corresponding new physics operators, in principle, can have any Lorentz structure. In this work, we perform a model independent analysis of new physics only in $b \rightarrow se^+e^-$ decay by considering effective operators either one at a time or two similar operators at a time. We include all the measurements in $b \rightarrow se^+e^-$ sector along with R_K/R_{K^*} in our analysis. We show that various new physics scenarios with vector/axial-vector operators can account for R_K/R_{K^*} data but those with scalar/pseudoscalar operators and with tensor operators can not. We also show that the azimuthal angular observable P_1 in $B \rightarrow K^*e^+e^-$ decay is most suited to discriminate between the different allowed solutions.

I. INTRODUCTION

The current measurements in $b \rightarrow s\ell^+\ell^-$ ($\ell = e, \mu$) sector show some significant tensions with the predictions of the Standard Model (SM). These include measurements of the lepton flavor universality (LFU) violating ratios R_K and R_{K^*} by the LHCb collaboration. In 2014, the LHCb collaboration reported the first measurement of the ratio $R_K \equiv \Gamma(B^+ \rightarrow K^+\mu^+\mu^-)/\Gamma(B^+ \rightarrow K^+e^+e^-)$ in the di-lepton invariant mass-squared, q^2 , range $1.1 \leq q^2 \leq 6.0 \text{ GeV}^2$ [1]. The measured value $0.745^{+0.090}_{-0.074}(\text{stat.}) \pm 0.036(\text{syst.})$ deviates from the SM prediction of ≈ 1 [2–4] by 2.6σ . Including the Run-II data and an update of the Run-I analysis, the value of R_K was updated in Moriond-2019. The updated value $0.846^{+0.060}_{-0.054}(\text{stat.})^{+0.016}_{-0.014}(\text{syst.})$ [5] is still $\simeq 2.5\sigma$ away from the SM.

The hint of LFU violation is further observed in another flavor ratio R_{K^*} . This ratio $R_{K^*} \equiv \Gamma(B^0 \rightarrow K^{*0}\mu^+\mu^-)/\Gamma(B^0 \rightarrow K^{*0}e^+e^-)$ was measured in the low ($0.045 \leq q^2 \leq 1.1 \text{ GeV}^2$) as well as in the central ($1.1 \leq q^2 \leq 6.0 \text{ GeV}^2$) q^2 bins by the LHCb collaboration [6]. The measured values are

*Electronic address: akalok@iitj.ac.in

†Electronic address: ksuman@iisc.ac.in

‡Electronic address: saini.1@iitj.ac.in

§Electronic address: uma@phy.iitb.ac.in

$0.660_{-0.070}^{+0.110}(\text{stat.}) \pm 0.024(\text{syst.})$ for the low q^2 bin and $0.685_{-0.069}^{+0.113}(\text{stat.}) \pm 0.047(\text{syst.})$ for the central q^2 bin. These measurements differ from the SM predictions of $R_{K^*}^{\text{low}} = 0.906 \pm 0.028$ and $R_{K^*}^{\text{central}} = 1.00 \pm 0.01$ [3] by $\sim 2.5\sigma$ and $\sim 3\sigma$, respectively. Later Belle collaboration announced their first results on the measurements of R_{K^*} in different q^2 bins for both B^0 and B^+ decay modes [7]. The measured values suffer from large statistical uncertainties and hence consistent with the SM predictions. The ratios R_K and R_{K^*} are essentially free from the hadronic uncertainties, making them extremely sensitive to new physics (NP) in $b \rightarrow se^+e^-$ or/and $b \rightarrow s\mu^+\mu^-$ transition(s).

Further, there are a few anomalous measurements which are related to possible NP in $b \rightarrow s\mu^+\mu^-$ transition only. These include measurements of angular observables, in particular P'_5 , in $B \rightarrow K^* \mu^+ \mu^-$ decay [8–10] and the branching ratio of $B_s \rightarrow \phi \mu^+ \mu^-$ [11]. By virtue of these measurements, it is natural to assume NP only in the muon sector to accommodate all $b \rightarrow s\ell^+\ell^-$ data. A large number of global analyses of $b \rightarrow s\ell^+\ell^-$ data have been performed under this assumption [12–18]. NP amplitude in $b \rightarrow s\mu^+\mu^-$ must have destructive interference with the SM amplitude to account for $R_K, R_{K^*} < 1$. Hence the NP operators in this sector are constrained to be in vector/axial-vector form. The global analyses found three different combinations of such operators which can account for all the data. Possible methods to distinguish between these allowed NP solutions are investigated in refs. [19–22]. However, the predicted value of $R_{K^*}^{\text{low}}$ for the solutions with NP only in $b \rightarrow s\mu^+\mu^-$ still differs significantly from the measured value. This requires presence of NP in $b \rightarrow se^+e^-$ along with $b \rightarrow s\mu^+\mu^-$, see for e.g, [23, 24].

While the LFU ratios R_K and R_{K^*} are theoretically clean, other observables in $b \rightarrow s\mu^+\mu^-$ sector which show discrepancy with SM, in particular the angular observables $B \rightarrow K^* \mu^+ \mu^-$ and $B_s \rightarrow \phi \mu^+ \mu^-$, are subject to significant hadronic uncertainties dominated by undermined power corrections. So far, the power corrections can be estimated only in the inclusive decays. For exclusive decays, there are no theoretical description of power corrections within QCD factorization and SCET framework. The possible NP effects in these observables can be masked by such corrections. The disagreement with the SM depends upon the guess value of power corrections. Under the assumption of $\sim 10\%$ non-factorisable power corrections in the SM predictions, the measurements of these observables show deviations from the SM at the level of $3\text{--}4\sigma$. However, if one assumes a sizable non-factorisable power corrections, the experimental data can be accommodated within the SM itself [25–28]. It is therefore expected that these tensions might stay unexplained until Belle-II can measure the corresponding observables in the inclusive $b \rightarrow s\mu^+\mu^-$ modes [26].

Therefore, if one considers the discrepancies in clean observables in $b \rightarrow s\ell^+\ell^-$ sector, which are R_K and R_{K^*} , then NP only in $b \rightarrow se^+e^-$ is as natural solution as NP in $b \rightarrow s\mu^+\mu^-$ sector. In this

work, we consider this possibility and perform a model independent analysis with NP restricted to $b \rightarrow se^+e^-$ sector. To the best of our knowledge, this is the first work where NP only in $b \rightarrow se^+e^-$ transition is considered in a model independent manner. In this scenario, we need the NP operators to increase the denominators of R_K and R_{K^*} . Hence, the need for interference with SM amplitude is no longer operative. We consider NP in the form of vector/axial-vector (V/A), scalar/pseudoscalar (S/P) and tensor (T) operators. We show that solutions based on V/A operators predict values of R_K/R_{K^*} , including $R_{K^*}^{\text{low}}$, which are in good agreement with the measured values. The scalar NP operators can account for the reduction in R_K but not in R_{K^*} and hence are ruled out. The coefficients of pseudoscalar operators are very severely constrained by the current bound on the branching ratio of $B_s \rightarrow e^+e^-$ and these operators do not lead to a reduction of R_K/R_{K^*} . It is not possible to get a solution to the R_K/R_{K^*} problem using only tensor operators [29] but a solution is possible in the form of a combination of V/A and T operators, as shown in ref. [30]. In this work, we will limit ourselves to solutions involving either one NP operator or two similar NP operators at a time. We will not consider solutions with two or more dissimilar operators.

The paper is organized as follows. In Sec. II, we discuss the methodology adopted in this work. The fit results for NP in the form of V/A operators are shown in Sec. III. In Sec. III A, we discuss methods to discriminate between different V/A solutions and comment on the most effective angular observables which can achieve this discrimination. Finally, we present our conclusions in Sec. IV.

II. METHODOLOGY

We analyze the R_K/R_{K^*} anomalies within the framework of effective field theory by assuming NP only in $b \rightarrow se^+e^-$ transition. We intend to identify the set of operators which can account for the measurements of R_K/R_{K^*} . We consider NP in the form of V/A, S/P and T operators and analyze scenarios with either one NP operator (1D) at a time or two similar NP operators (2D) at a time.

In the SM, the effective Hamiltonian for $b \rightarrow sl^+\ell^-$ transition is

$$\begin{aligned} \mathcal{H}^{\text{SM}} = & -\frac{4G_F}{\sqrt{2}\pi} V_{ts}^* V_{tb} \left[\sum_{i=1}^6 C_i(\mu) \mathcal{O}_i(\mu) + C_7 \frac{e}{16\pi^2} [\bar{s}\sigma_{\mu\nu}(m_s P_L + m_b P_R)b] F^{\mu\nu} \right. \\ & \left. + C_9 \frac{\alpha_{em}}{4\pi} (\bar{s}\gamma^\mu P_L b)(\bar{\ell}\gamma_\mu \ell) + C_{10} \frac{\alpha_{em}}{4\pi} (\bar{s}\gamma^\mu P_L b)(\bar{\ell}\gamma_\mu \gamma_5 \ell) \right], \end{aligned} \quad (1)$$

where G_F is the Fermi constant, V_{ts} and V_{tb} are the Cabibbo-Kobayashi-Maskawa (CKM) matrix elements and $P_{L,R} = (1 \mp \gamma^5)/2$ are the projection operators. The effect of the operators \mathcal{O}_i , $i =$

1–6, 8 can be embedded in the redefined effective Wilson coefficients (WCs) as $C_7(\mu) \rightarrow C_7^{\text{eff}}(\mu, q^2)$ and $C_9(\mu) \rightarrow C_9^{\text{eff}}(\mu, q^2)$.

We now add following NP contributions to the SM effective Hamiltonian,

$$\begin{aligned} \mathcal{H}_{\text{VA}}^{\text{NP}} = & -\frac{\alpha_{\text{em}} G_F}{\sqrt{2}\pi} V_{ts}^* V_{tb} \left[C_9^{\text{NP},e} (\bar{s}\gamma^\mu P_L b) (\bar{e}\gamma_\mu e) + C_{10}^{\text{NP},e} (\bar{s}\gamma^\mu P_L b) (\bar{e}\gamma_\mu \gamma_5 e) \right. \\ & \left. + C_9^{\prime,e} (\bar{s}\gamma^\mu P_R b) (\bar{e}\gamma_\mu e) + C_{10}^{\prime,e} (\bar{s}\gamma^\mu P_R b) (\bar{e}\gamma_\mu \gamma_5 e) \right], \end{aligned} \quad (2)$$

$$\begin{aligned} \mathcal{H}_{\text{SP}}^{\text{NP}} = & -\frac{\alpha_{\text{em}} G_F}{\sqrt{2}\pi} V_{ts}^* V_{tb} [C_{SS}^e (\bar{s}b)(\bar{e}e) + C_{SP}^e (\bar{s}b)(\bar{e}\gamma_5 e) \\ & + C_{PS}^e (\bar{s}\gamma_5 b)(\bar{e}e) + C_{PP}^e (\bar{s}\gamma_5 b)(\bar{e}\gamma_5 e)], \end{aligned} \quad (3)$$

$$\mathcal{H}_{\text{T}}^{\text{NP}} = -\frac{\alpha_{\text{em}} G_F}{\sqrt{2}\pi} V_{ts}^* V_{tb} [C_T^e (\bar{s}\sigma^{\mu\nu} b) (\bar{e}\sigma_{\mu\nu} e) + C_{T5}^e (\bar{s}\sigma^{\mu\nu} b) (\bar{e}\sigma_{\mu\nu} \gamma_5 e)], \quad (4)$$

where $C_{9,10}^{\text{NP},e}$, $C_{9,10}^{\prime,e}$, and $C_{SS,SP,PS,PP,T,T5}^e$ are the NP WCs.

Using simple symmetry arguments, we can argue that S/P operators can not provide a solution to R_K/R_{K^*} discrepancy. The operators containing the quark bilinear $\bar{s}b$ can lead to $B \rightarrow Ke^+e^-$ transition but not $B \rightarrow K^*e^+e^-$ transition. Such operators can account for R_K but not R_{K^*} . On the other hand, the operators containing the quark pseudoscalar bilinear $\bar{s}\gamma_5 b$ can not lead to $B \rightarrow Ke^+e^-$. These operators can not account for R_K . In addition, the contribution of these operators to $B_s \rightarrow e^+e^-$ is not subject to helicity suppression. Hence, the coefficients C_{PS}^e and C_{PP}^e are constrained to be very small. The current upper limit on $\mathcal{B}(B_s \rightarrow e^+e^-) < 9.4 \times 10^{-9}$ at 90% C.L., leads to the condition

$$|C_{PS}^e|^2 + |C_{PP}^e|^2 \lesssim 0.01, \quad (5)$$

whereas one needs

$$120 \lesssim |C_{PS}^e|^2 + |C_{PP}^e|^2 \lesssim 345, \quad 9 \lesssim |C_{PS}^e|^2 + |C_{PP}^e|^2 \lesssim 29, \quad (6)$$

to satisfy the experimental constraint on $R_{K^*}^{\text{low}}$ and $R_{K^*}^{\text{central}}$ respectively. Therefore, we will not consider S/P operators in our fit procedure.

The NP Hamiltonian can potentially impact observables in the decays induced by the quark level transition $b \rightarrow se^+e^-$. To obtain the values of NP WCs, we perform a fit to the current data in $b \rightarrow se^+e^-$ sector. We consider following fifteen observables in our fit:

- Measured values of R_K in $1.1 \leq q^2 \leq 6.0$ GeV² bin [5] and R_{K^*} in both $0.045 < q^2 < 1.1$ GeV² and $1.1 < q^2 < 6.0$ GeV² bins by the LHCb collaboration [6],
- Measured values of R_{K^*} by the Belle collaboration in $0.045 < q^2 < 1.1$ GeV², $1.1 < q^2 < 6.0$ GeV² and $15.0 < q^2 < 19.0$ GeV² bins for both B^0 and B^+ decay modes [7],

- The upper limit of $\mathcal{B}(B_s \rightarrow e^+e^-) < 9.4 \times 10^{-9}$ at 90% C.L. by the LHCb collaboration [31],
- The differential branching fraction of $B \rightarrow K^*e^+e^-$, $(3.1_{-0.8}^{+0.9} \pm 0.2) \times 10^{-7}$, in $0.001 < q^2 < 1.0$ GeV^2 bin by the LHCb collaboration [32],
- The measured value of K^* longitudinal polarization fraction, $0.16 \pm 0.06 \pm 0.03$, in $0.002 < q^2 < 1.12$ GeV^2 bin by the LHCb collaboration [33],
- Measured values of the branching ratios of $B \rightarrow X_s e^+e^-$ by the BaBar collaboration in both $1.0 < q^2 < 6.0$ GeV^2 and $14.2 < q^2 < 25.0$ GeV^2 bins which are $(1.93_{-0.45}^{+0.47+0.21} \pm 0.18) \times 10^{-6}$ and $(0.56_{-0.18}^{+0.19+0.03}) \times 10^{-6}$, respectively [34],
- Measured values of P'_4 in $B \rightarrow K^*e^+e^-$ decay by the Belle collaboration in $1.0 < q^2 < 6.0$ GeV^2 and $14.18 < q^2 < 19.0$ GeV^2 bins which are $-0.72_{-0.39}^{+0.40} \pm 0.06$ and $-0.15_{-0.40}^{+0.41} \pm 0.04$, respectively [35],
- Measured values of P'_5 in $B \rightarrow K^*e^+e^-$ decay by the Belle collaboration in $1.0 < q^2 < 6.0$ GeV^2 and $14.18 < q^2 < 19.0$ GeV^2 bins which are $-0.22_{-0.41}^{+0.39} \pm 0.03$ and $-0.91_{-0.30}^{+0.36} \pm 0.03$, respectively [35].

We define the χ^2 function as

$$\chi^2(C_i) = \sum_{\text{all obs.}} \frac{(O^{\text{th}}(C_i) - O^{\text{exp}})^2}{\sigma_{\text{exp}}^2 + \sigma_{\text{th}}^2}. \quad (7)$$

Here $O^{\text{th}}(C_i)$ are the theoretical predictions of the observables taken into fit which depend on the NP WCs and O^{exp} are the measured central values of the corresponding observables. The σ_{exp} and σ_{th} are the experimental and theoretical uncertainties, respectively. The experimental errors in all observables dominate over the theoretical errors. In case of the asymmetric errors, we use the larger error in our analysis. The prediction of $O^{\text{th}}(C_i)$ is obtained using `Flavio` package [36] which uses the most precise form factor predictions obtained in the light cone sum rule (LCSR) [37, 38] approach. The non-factorisable corrections are incorporated following the parameterization used in Ref. [36, 37]. These are also compatible with the calculations in Ref. [39].

We obtain the values of NP WCs by minimizing the χ^2 using CERN minimization code `Minuit` [40, 41]. We perform the minimization in two ways: (a) one NP operator at a time and (b) two NP operators at a time. Since we do the fit with fifteen data points, it is expected that an NP scenario with a value of $\chi_{\text{min}}^2 \approx 15$ provides a good fit to the data. We also define $\text{pull} = \sqrt{\Delta\chi^2}$ where $\Delta\chi^2 = (\chi_{\text{SM}}^2 - \chi_{\text{min}}^2)$. Since $\chi_{\text{SM}}^2 \approx 27$, any scenario with $\text{pull} \gtrsim 3.0$ can be

considered to be a viable solution. In the next section, we present our fit results and discuss them in details.

III. VECTOR/AXIAL-VECTOR NEW PHYSICS

There are four cases for one operator fit and six cases for two operators fit. For all of these cases, we list the best fit values of WCs in Table I along with their χ_{\min}^2 values. We also calculate the corresponding values of pull which determine the degree of improvement over the SM.

Wilson Coefficient(s)	Best fit value(s)	χ_{\min}^2	pull
$C_i = 0$ (SM)	–	27.42	
1D Scenarios			
$C_9^{\text{NP},e}$	0.91 ± 0.28	15.21	3.5
$C_{10}^{\text{NP},e}$	-0.86 ± 0.25	12.60	3.8
$C_9^{\prime,e}$	0.24 ± 0.24	26.40	1.0
$C_{10}^{\prime,e}$	-0.17 ± 0.21	26.70	0.8
2D Scenarios			
$(C_9^{\text{NP},e}, C_{10}^{\text{NP},e})$	$(-1.03, -1.42)$	11.57	3.9
$(C_9^{\text{NP},e}, C_9^{\prime,e})$	$(-3.61, -4.76)$	17.65	3.1
	$(-3.52, 4.29)$	15.71	3.4
	$(1.21, -0.54)$	12.83	3.8
$(C_9^{\text{NP},e}, C_{10}^{\prime,e})$	$(1.21, 0.69)$	12.39	3.9
$(C_9^{\prime,e}, C_{10}^{\text{NP},e})$	$(-0.50, -1.03)$	11.30	4.0
$(C_9^{\prime,e}, C_{10}^{\prime,e})$	$(2.05, 2.33)$	10.41	4.1
	$(-2.63, -1.86)$	12.71	3.8
$(C_{10}^{\text{NP},e}, C_{10}^{\prime,e})$	$(3.64, 5.33)$	18.50	3.0
	$(-1.04, 0.38)$	11.14	4.0
	$(4.56, -5.24)$	16.58	3.3

Table I: The best fit values of NP WCs in $b \rightarrow se^+e^-$ transition for 1D and 2D scenarios. The value of χ_{SM}^2 is 27.42.

From Table I, we find that the $C_9^{\text{NP},e}$ and $C_{10}^{\text{NP},e}$ scenarios provide a good fit to the $b \rightarrow se^+e^-$ data. However, the other two 1D scenarios, $C_9^{\prime,e}$ and $C_{10}^{\prime,e}$, fail to provide any improvement over the SM. Therefore, we reject them on the basis of $\Delta\chi^2$ or pull. In the case of 2D framework, all six combinations improve the global fit as compared to the SM.

We now impose the stringent condition that a NP solution must predict the values of R_K , $R_{K^*}^{\text{low}}$ and $R_{K^*}^{\text{central}}$ to be within 1σ of their measured values. In order to identify solutions satisfying this condition, we calculate the predictions of R_K/R_{K^*} for all good fit scenarios. The predicted values of these quantities are listed in Table II from which we observe that the 1D scenario C_9^{NP} could not accommodate both the $R_{K^*}^{\text{low}}$ and $R_{K^*}^{\text{central}}$ within 1σ whereas most of the other solutions fail to explain the 1σ range of $R_{K^*}^{\text{low}}$ only. There are only three 2D solutions whose predictions for R_K , $R_{K^*}^{\text{low}}$ and $R_{K^*}^{\text{central}}$ are within 1σ of their measurements. We call these scenarios as allowed NP solutions and list them in Table III. The 1σ and 2σ allowed regions for these three allowed solutions are shown in Fig 1.

Wilson Coefficient(s)	Best fit value(s)	pull	R_K	$R_{K^*}^{\text{low}}$	$R_{K^*}^{\text{central}}$
Expt. 1σ range			[0.784, 0.908]	[0.547, 0.773]	[0.563, 0.807]
1D Scenarios					
$C_9^{\text{NP},e}$	0.91 ± 0.28	3.5	0.806 ± 0.001	0.883 ± 0.008	0.832 ± 0.009
$C_{10}^{\text{NP},e}$	-0.86 ± 0.25	3.8	0.805 ± 0.005	0.855 ± 0.007	0.778 ± 0.012
2D Scenarios					
$(C_9^{\text{NP},e}, C_{10}^{\text{NP},e})$	$(-1.03, -1.42)$	3.9	0.825 ± 0.011	0.832 ± 0.007	0.745 ± 0.026
$(C_9^{\text{NP},e}, C_9^{\prime,e})$	$(-3.61, -4.76)$	3.1	0.867 ± 0.050	0.757 ± 0.007	0.625 ± 0.024
	$(-3.52, 4.29)$	3.4	0.832 ± 0.001	0.798 ± 0.028	0.707 ± 0.090
	$(1.21, -0.54)$	3.8	0.853 ± 0.001	0.825 ± 0.018	0.701 ± 0.012
$(C_9^{\text{NP},e}, C_{10}^{\prime,e})$	$(1.21, 0.69)$	3.9	0.855 ± 0.004	0.819 ± 0.016	0.691 ± 0.011
$(C_9^{\prime,e}, C_{10}^{\text{NP},e})$	$(-0.50, -1.03)$	4.0	0.844 ± 0.007	0.812 ± 0.012	0.690 ± 0.009
$(C_9^{\prime,e}, C_{10}^{\prime,e})$	$(2.05, 2.33)$	4.1	0.845 ± 0.010	0.808 ± 0.014	0.683 ± 0.029
	$(-2.63, -1.86)$	3.8	0.856 ± 0.020	0.808 ± 0.015	0.684 ± 0.010
$(C_{10}^{\text{NP},e}, C_{10}^{\prime,e})$	$(3.64, 5.33)$	3.0	0.860 ± 0.015	0.788 ± 0.014	0.645 ± 0.015
	$(-1.04, 0.38)$	4.0	0.846 ± 0.004	0.809 ± 0.013	0.686 ± 0.014
	$(4.56, -5.24)$	3.3	0.842 ± 0.004	0.809 ± 0.015	0.685 ± 0.019

Table II: The predictions of R_K , $R_{K^*}^{\text{low}}$ and $R_{K^*}^{\text{central}}$ for the good fit scenarios obtained in Table. I.

After identifying the allowed solutions, we find out the set of observables which can discriminate between them. In the next subsection, we investigate discriminating capabilities of the standard angular observables in $B \rightarrow K^* e^+ e^-$ decay.

Solution	Wilson Coefficient(s)	Best fit value(s)	pull	R_K	$R_{K^*}^{\text{low}}$	$R_{K^*}^{\text{central}}$
Expt. 1σ range				[0.784, 0.908]	[0.547, 0.773]	[0.563, 0.807]
2D Scenarios						
I	$(C_9^{\text{NP},e}, C_9^{\prime,e})$	(-3.61, -4.76)	3.1	0.867 ± 0.050	0.757 ± 0.007	0.625 ± 0.024
II		(-3.52, 4.29)	3.4	0.832 ± 0.001	0.798 ± 0.028	0.707 ± 0.090
III	$(C_{10}^{\text{NP},e}, C_{10}^{\prime,e})$	(3.64, 5.33)	3.0	0.860 ± 0.015	0.788 ± 0.014	0.645 ± 0.015

Table III: Here we list only those NP WCs which generate R_K and R_{K^*} within 1σ range of their experimental values.

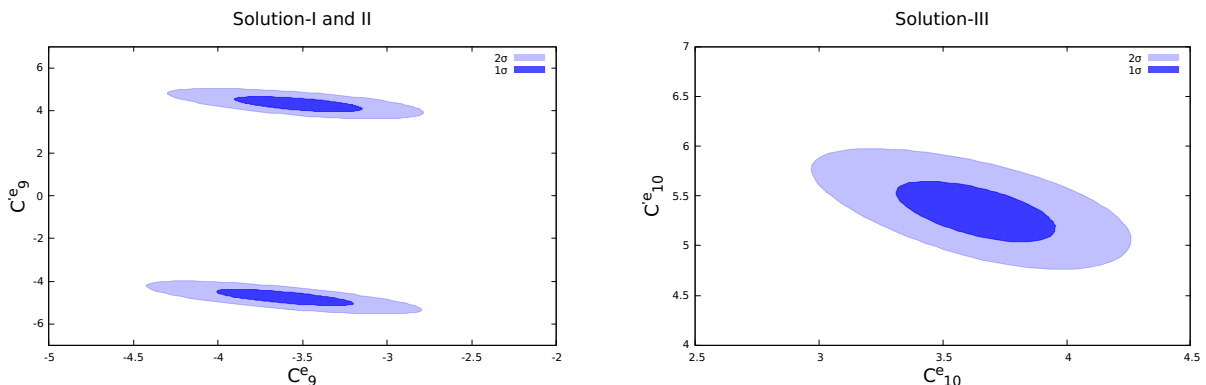


Figure 1: The allowed 1σ and 2σ ellipses for the three 2D solutions listed in Table III.

A. Discriminating V/A solutions

The differential distribution of the four-body decay $B \rightarrow K^*(\rightarrow K\pi)e^+e^-$ can be parametrized as the function of one kinematic and three angular variables. The kinematic variable is $q^2 = (p_B - p_{K^*})^2$, where p_B and p_{K^*} are respective four-momenta of B and K^* mesons. The angular variables are defined in the K^* rest frame. They are (a) θ_K the angle between B and K mesons where K meson comes from K^* decay, (b) θ_e the angle between momenta of e^- and B meson and (c) ϕ the angle between K^* decay plane and the plane defined by the $e^+ - e^-$ momenta. The full decay distribution can be expressed as [42, 43]

$$\frac{d^4\Gamma}{dq^2 d\cos\theta_e d\cos\theta_K d\phi} = \frac{9}{32\pi} I(q^2, \theta_e, \theta_K, \phi), \quad (8)$$

where

$$\begin{aligned}
I(q^2, \theta_e, \theta_K, \phi) = & I_1^s \sin^2 \theta_K + I_1^c \cos^2 \theta_K + (I_2^s \sin^2 \theta_K + I_2^c \cos^2 \theta_K) \cos 2\theta_e \\
& + I_3 \sin^2 \theta_K \sin^2 \theta_e \cos 2\phi + I_4 \sin 2\theta_K \sin 2\theta_e \cos \phi \\
& + I_5 \sin 2\theta_K \sin \theta_e \cos \phi \\
& + (I_6^s \sin^2 \theta_K + I_6^c \cos^2 \theta_K) \cos \theta_e + I_7 \sin 2\theta_K \sin \theta_e \sin \phi \\
& + I_8 \sin 2\theta_K \sin 2\theta_e \sin \phi + I_9 \sin^2 \theta_K \sin^2 \theta_e \sin 2\phi.
\end{aligned} \tag{9}$$

The twelve angular coefficients $I_i^{(a)}$ depend on q^2 and on various hadron form factors. The detailed expressions of these coefficients can be found in Ref. [43]. The corresponding expression for the CP conjugate decay can be obtained by replacing θ_e by $(\pi - \theta_e)$ and ϕ by $-\phi$. This leads to the following transformations of angular coefficients

$$I_{1,2,3,4,7}^{(a)} \implies \bar{I}_{1,2,3,4,7}^{(a)}, \quad I_{5,6,8,9}^{(a)} \implies -\bar{I}_{5,6,8,9}^{(a)}, \tag{10}$$

where $\bar{I}_i^{(a)}$ are the complex conjugate of $I_i^{(a)}$. Therefore, there could be twelve CP averaged angular observables which can be defined as [42, 43]

$$S_i^{(a)}(q^2) = \frac{I_i^{(a)}(q^2) + \bar{I}_i^{(a)}(q^2)}{d(\Gamma + \bar{\Gamma})/dq^2}. \tag{11}$$

The longitudinal polarization fraction of K^* , F_L , depends on the distribution of the events in the angle θ_K (after integrating over θ_e and ϕ) and the forward-backward asymmetry, A_{FB} , is defined in terms of θ_e (after integrating over θ_K and ϕ). We can write these two quantities in terms of $S_i^{(a)}$ as follows

$$A_{FB} = \frac{3}{8} (2S_6^s + S_6^c), \quad F_L = -S_2^c. \tag{12}$$

In addition to the S_i observables, one can also investigate the NP effects on a set of optimized observables P_i . In fact, the observables P_i are theoretically cleaner in comparison to the form factors dependent observables S_i . These two sets of observables are related to each other through the following relations [44]

$$\begin{aligned}
P_1 &= \frac{2S_3}{1 - F_L}, \quad P_2 = \frac{S_6^s}{2(1 - F_L)}, \quad P_3 = \frac{-S_9}{1 - F_L}, \\
P_4 &= \frac{2S_4}{\sqrt{F_L(1 - F_L)}}, \quad P_5 = \frac{S_5}{\sqrt{F_L(1 - F_L)}}, \quad P_6 = \frac{-S_7}{\sqrt{F_L(1 - F_L)}}, \quad P_8 = \frac{-2S_8}{\sqrt{F_L(1 - F_L)}}.
\end{aligned} \tag{13}$$

Observable	q^2 bin	SM	S-I	S-II	S-III
A_{FB}	[1.1, 6]	0.008 ± 0.031	-0.146 ± 0.026	-0.161 ± 0.027	-0.016 ± 0.011
	[15, 19]	0.368 ± 0.018	-0.005 ± 0.003	0.002 ± 0.005	0.026 ± 0.004
F_L	[1.1, 6]	0.764 ± 0.043	0.630 ± 0.056	0.599 ± 0.055	0.765 ± 0.042
	[15, 19]	0.341 ± 0.020	0.338 ± 0.022	0.325 ± 0.020	0.349 ± 0.020

Table IV: Average values of $B \rightarrow K^* e^+ e^-$ angular observables A_{FB} and F_L in SM as well as for the allowed NP V/A solutions listed in Table. III.

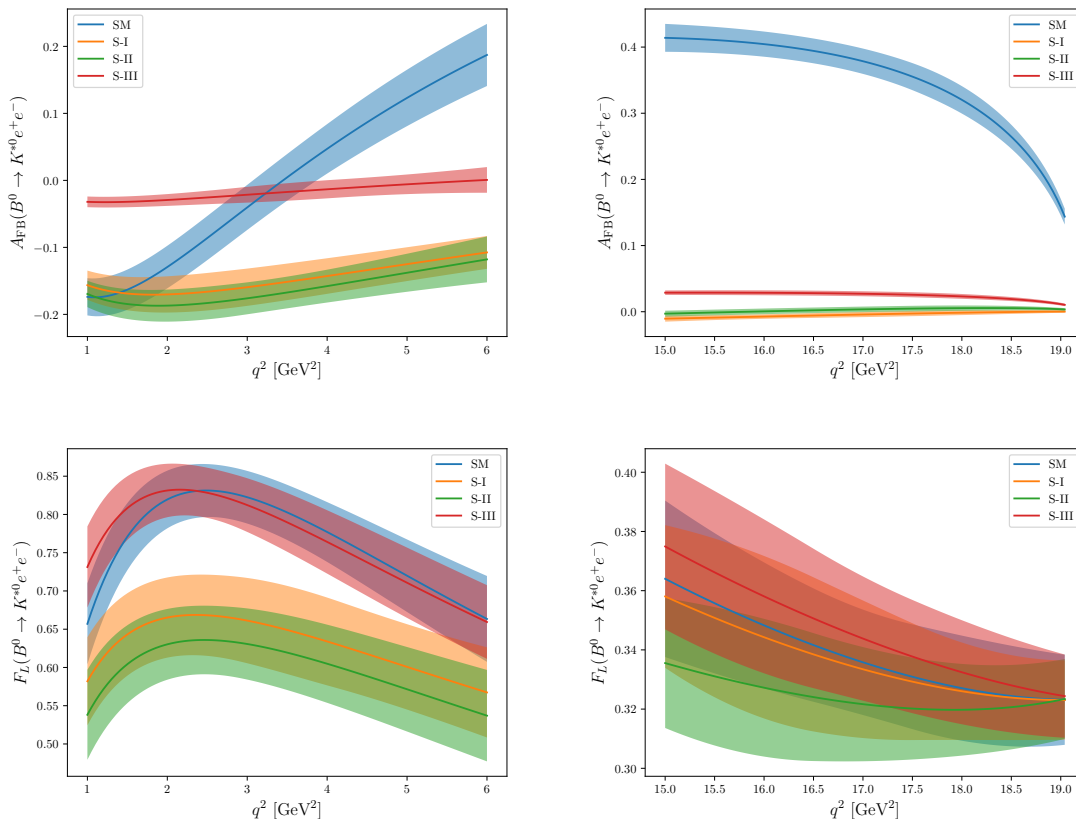


Figure 2: Plots of A_{FB} and F_L as a function of q^2 for the SM and the three NP V/A solutions. The left and right panels correspond to the low ([1.1, 6.0] GeV²) and high ([15, 19] GeV²) q^2 bins, respectively.

We calculate A_{FB} , F_L along with optimized observables $P_{1,2,3}$ and $P'_{4,5,6,8}$ for the SM and the three allowed NP solutions in $q^2 \in [1.1, 6.0]$ and $[15, 19]$ GeV² bins. The average values of A_{FB} and F_L are listed in Table IV and the q^2 plots are shown in Fig. 2. From the predictions, we observe the following features:

- In low q^2 region, the SM prediction of $A_{FB}(q^2)$ has a zero crossing at ~ 3.5 GeV². For the NP solutions, the predictions are negative throughout the low q^2 range. However, the

$A_{FB}(q^2)$ curve is almost the same for S-I and S-II whereas for S-III, it is markedly different. Therefore an accurate measurement of q^2 distribution of A_{FB} can discriminate between S-III and the remaining two NP solutions.

- In high q^2 region, the SM prediction of A_{FB} is 0.368 ± 0.018 whereas the predictions for the three solutions are almost zero. If A_{FB} in high q^2 region is measured to be small, it provides additional confirmation for the existence of NP, which is indicated by the reduced values of R_K and R_{K^*} . All the three NP solutions induce a large deviation in A_{FB} , but the discriminating capability of A_{FB} is extremely limited.
- The S-I and S-II scenarios can marginally suppress the value of F_L in low q^2 region compared to the SM whereas for S-III, the predicted value is consistent with the SM. In high q^2 region, F_L for all three scenarios are close to the SM value. Hence F_L cannot discriminate between the allowed V/A solutions.

Hence we see that neither A_{FB} nor F_L have the power to discriminate between all the three allowed V/A NP solutions. Therefore, we now study optimized observables P_i in $B \rightarrow K^* e^+ e^-$ decay. In particular, we investigate the distinguishing ability of $P_{1,2,3}$ and $P'_{4,5,6,8}$. We compute the average values of these seven observables for the SM along with three NP scenarios in two different q^2 bins, $q^2 \in [1.1, 6.0]$ and $[15, 19]$ GeV^2 . These are listed in Tab V. We also plot these observables as a function of q^2 for the SM and the three solutions. The q^2 plots for $P_{1,2,3}$ and $P'_{4,5,6,8}$ are illustrated in Figs. 3 and 4, respectively. From these figures and the table, it is apparent that

- The observable P_1 in the low q^2 region can discriminate between all three NP solutions, particularly S-I and S-II. The sign of P_1 is opposite for these scenarios. Hence an accurate measurement of P_1 can distinguish between S-I and S-II solutions. In fact, measurement of P_1 with an absolute uncertainty of 0.05 can confirm or rule out S-I and S-II solutions by more than 4σ . In the high- q^2 region, the predictions for all allowed solutions are consistent with the SM.
- The observable P_2 can be a good discriminant of S-III provided we have handle over its q^2 distribution in $[1.1, 6.0]$ GeV^2 bin. In this bin, $P_2(q^2)$ has a zero crossing at ~ 3.5 GeV^2 for the SM prediction whereas there is no zero crossing for any of the allowed solutions. Scenarios S-I and S-II predict large negative values for P_2 , around -0.3 whereas the S-III predicts

Observable	q^2 bin	SM	S-I	S-II	S-III
P_1	[1.1, 6]	-0.113 ± 0.032	0.507 ± 0.064	-0.627 ± 0.035	-0.291 ± 0.034
	[15, 19]	-0.623 ± 0.044	-0.602 ± 0.042	-0.609 ± 0.040	-0.700 ± 0.037
P_2	[1.1, 6]	0.023 ± 0.090	-0.263 ± 0.020	-0.267 ± 0.021	-0.046 ± 0.030
	[15, 19]	0.372 ± 0.013	-0.005 ± 0.004	0.002 ± 0.004	0.027 ± 0.004
P_3	[1.1, 6]	0.003 ± 0.008	0.018 ± 0.036	-0.017 ± 0.032	0.002 ± 0.006
	[15, 19]	-0.000 ± 0.000	-0.045 ± 0.004	0.045 ± 0.004	-0.000 ± 0.000
P'_4	[1.1, 6]	-0.352 ± 0.038	-0.256 ± 0.033	-0.605 ± 0.011	-0.447 ± 0.027
	[15, 19]	-0.635 ± 0.008	-0.631 ± 0.008	-0.632 ± 0.008	-0.650 ± 0.008
P'_5	[1.1, 6]	-0.440 ± 0.106	0.336 ± 0.060	0.358 ± 0.045	0.487 ± 0.079
	[15, 19]	-0.593 ± 0.036	-0.001 ± 0.005	-0.014 ± 0.006	-0.032 ± 0.005
P'_6	[1.1, 6]	-0.046 ± 0.102	-0.025 ± 0.053	-0.028 ± 0.066	-0.042 ± 0.093
	[15, 19]	-0.002 ± 0.001	-0.002 ± 0.001	-0.002 ± 0.001	-0.002 ± 0.001
P'_8	[1.1, 6]	-0.015 ± 0.035	-0.006 ± 0.032	0.012 ± 0.027	-0.009 ± 0.023
	[15, 19]	0.001 ± 0.000	0.036 ± 0.002	-0.036 ± 0.003	0.000 ± 0.000

Table V: Average values of $P_{1,2,3}$ and $P'_{4,5,6,8}$ in $B \rightarrow K^* e^+ e^-$ decay for the three V/A NP solutions listed in Table. III as well as for the SM.

relatively smaller negative values. Hence an accurate measurement of q^2 distribution of P_2 in [1.1, 6.0] GeV² bin can discriminate S-III with other two solutions. In high q^2 region, the predictions of P_2 for all three solutions are almost the same. These scenarios predict a large deviation from the SM. The SM prediction for P_2 is ~ 0.4 whereas all three solutions predict values closer to zero. Hence, an accurate measurement of the value of P_2 is a smoking-gun signal for the existence of NP in $b \rightarrow se^+e^-$ transition as the solution for the current R_K and R_{K^*} anomalies.

- The P_3 observable in the low- q^2 region cannot discriminate between the allowed solutions. However, in the high q^2 region, P_3 can uniquely discriminate the three solutions. In particular, the prediction of P_3 for S-III in the high q^2 is the same as the SM whereas the predictions for S-I and S-II are exactly equal and opposite.
- The P'_4 in low- q^2 region can only distinguish S-II solution from the other two NP solutions and the SM. In high- q^2 region, it has a poor discrimination capability.
- In the low q^2 bin, P'_5 has a zero crossing at ~ 2 GeV² and has an average negative value in the SM. For all three NP solutions, there is no zero crossing in P'_5 . Further, these scenarios

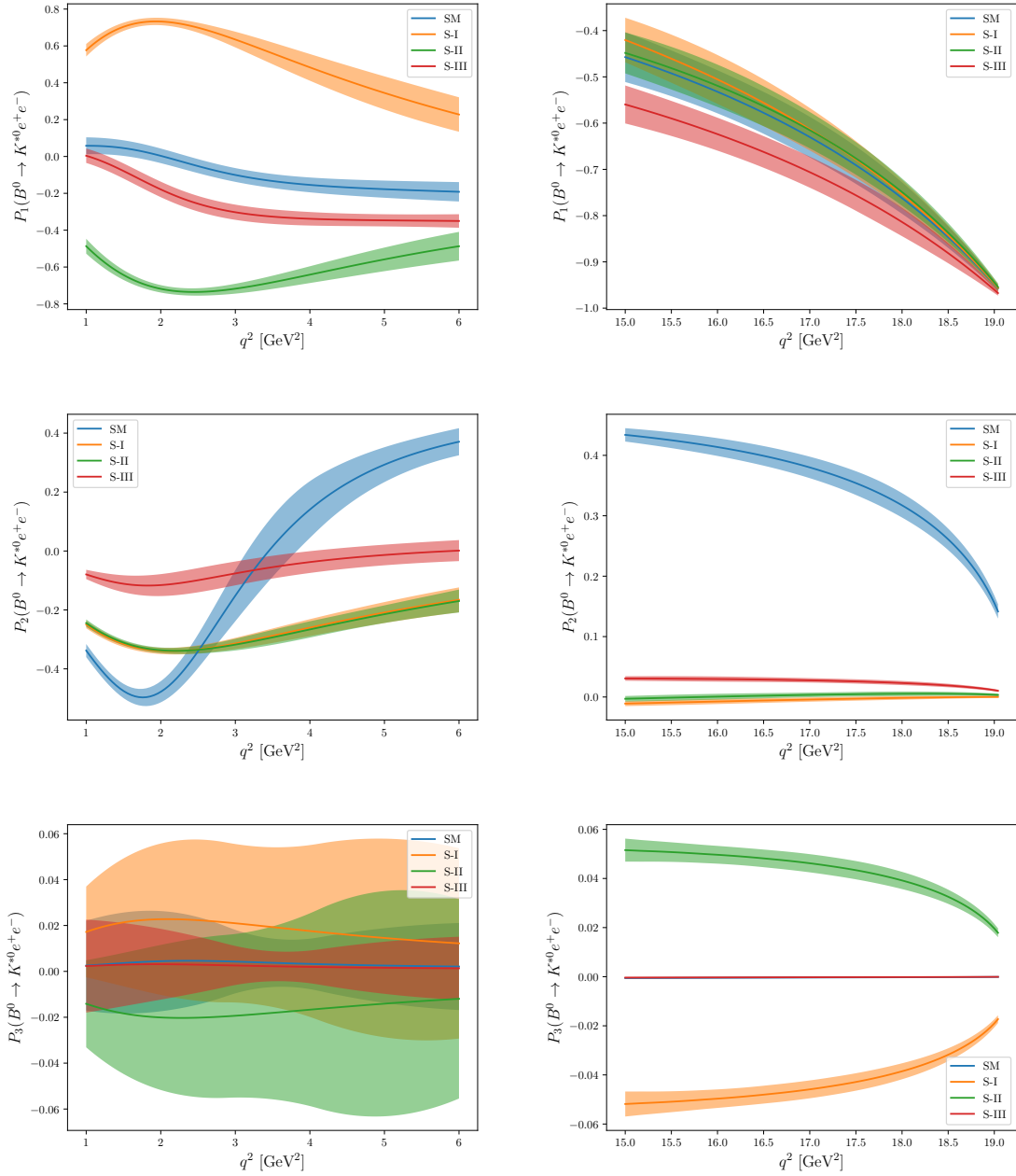


Figure 3: Plots of $P_{1,2,3}(q^2)$ as a function of q^2 for the SM and three NP scenarios. The left and right panels correspond to the low ($[1.1, 6.0] \text{ GeV}^2$) and high ($[15, 19] \text{ GeV}^2$) q^2 bins, respectively.

predict a large positive values. In the high q^2 region, the SM predicts a large negative value of P_5' whereas NP scenarios predict values close to zero. Thus we see that if we impose the condition that NP in $b \rightarrow se^+e^-$ should simultaneously generate R_K and R_{K^*} within 1σ of their measured values, it implies a large deviation in P_5' from the SM. This is reflected in the values of pull for the three allowed solutions which are relatively smaller than the other

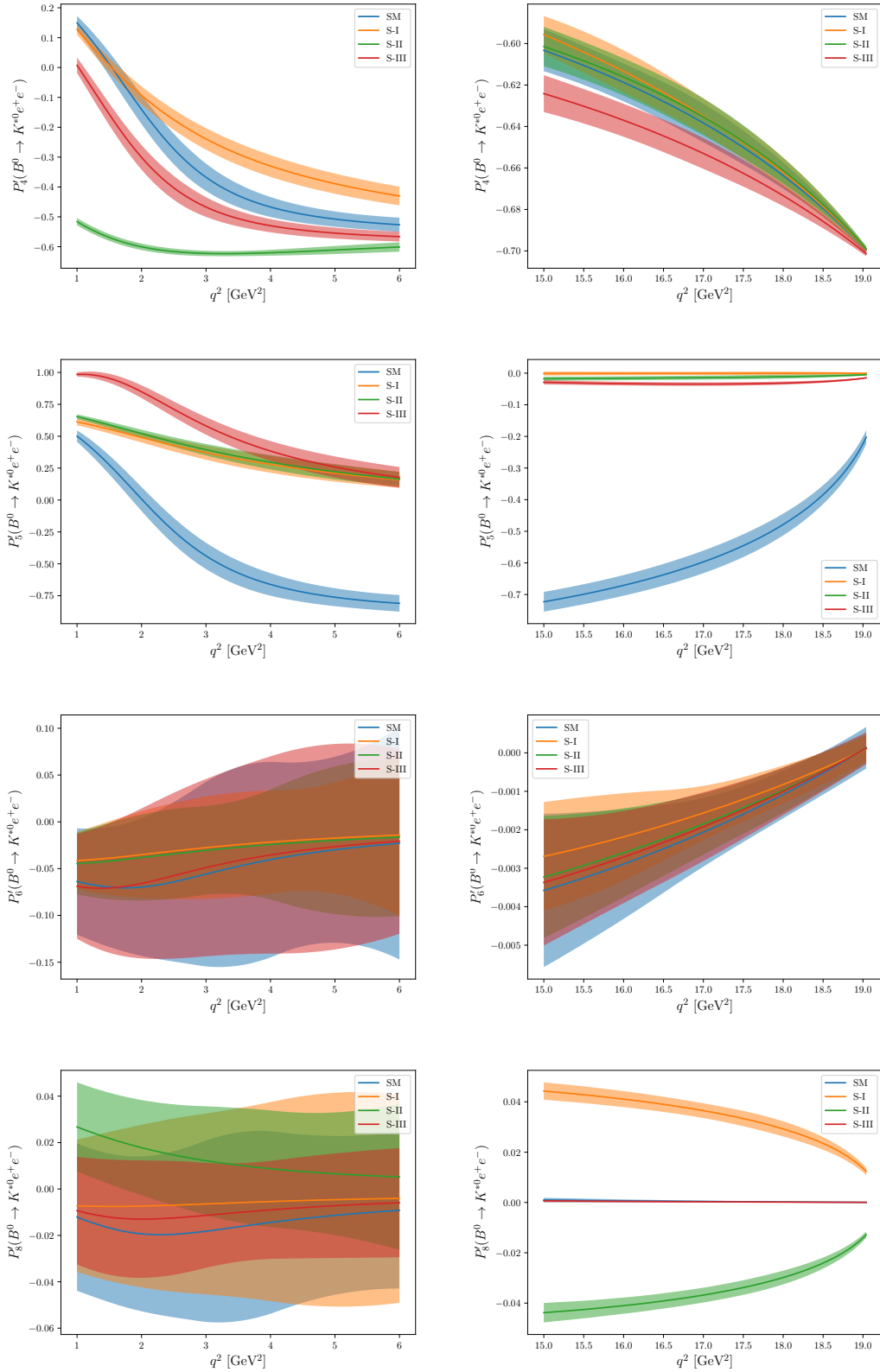


Figure 4: Plots of $P'_{4,5,6,8}(q^2)$ as a function of q^2 for the SM and three NP scenarios. The left and right panels correspond to the low $([1.1, 6.0] \text{ GeV}^2)$ and high $([15, 19] \text{ GeV}^2)$ q^2 bins respectively.

scenarios which fail to explain R_K and R_{K^*} simultaneously. The depletion in pull for these allowed solutions is due to inconsistency between the measured and predicted values of P'_5 .

- In the both low and high- q^2 regions, the NP predictions for P'_6 for all three scenarios are consistent with the SM.
- The P'_8 in the low- q^2 region does not have any discrimination capability. The predicted values for all solutions are consistent with the SM. In the high- q^2 region, both S-III and SM predict P'_8 values close to zero whereas S-I and S-II predict large positive and negative values, respectively.

From this detailed study of the behavior of the optimized observables P_i , we find that both P_1 and P'_4 at low- q^2 have the best capability to discriminate between all the three V/A solutions. The predicted values of P_1 are equal and opposite for S-I and S-II and of a much smaller magnitude for S-III. Moreover, each of the predicted values is appreciably different from the SM prediction. Their magnitudes are quite large $\sim (0.3 - 0.6)$ with a relative theoretical uncertainty of about 10%. Hence, a measurement of the variable P_1 , with an experimental uncertainty of about 0.05, will not only confirm the presence of new physics in the $b \rightarrow se^+e^-$ amplitude but also can determine the correct WC of the NP operators. In the case P'_4 , the predictions of all the three solutions have the same sign but their magnitudes are quite different. The theoretical uncertainty in the predictions is quite low too. So, P'_4 observable also has a good capability to distinguish between the three V/A solutions.

IV. CONCLUSIONS

In this work, we intend to analyze $R_{K^{(*)}}$ anomalies by assuming NP only in $b \rightarrow se^+e^-$ decay. The effects of possible NP are encoded in the WCs of effective operators with different Lorentz structures. These WCs are constrained using all measurements in the $b \rightarrow se^+e^-$ sector along with lepton-universality-violating ratios R_K/R_{K^*} . We show that scalar/pseudoscalar NP operators and tensor NP operators can not explain the data in $b \rightarrow se^+e^-$ sector. We consider NP in the form of V/A operators, either one operator at a time or two similar operators at a time. We find that there are several scenarios which can provide a good fit to the data. However, there are only three solutions whose predictions of R_K/R_{K^*} , including R_{K^*} in the in the low- q^2 bin ($0.045 \text{ GeV}^2 \leq q^2 \leq 1.1 \text{ GeV}^2$), match the data well. In order to discriminate between the three allowed V/A solutions, we consider several angular observables in the $B \rightarrow K^*e^+e^-$ decay. The

three solutions predict very different values for the optimized observables P_1 and P'_4 in the low- q^2 bin. Both these observables also have the additional advantage that the theoretical uncertainties in their predictions are less than 10%. Hence a measurement of either of these observables, to an absolute uncertainty of 0.05, can lead to a unique identification of one of the solutions..

Acknowledgement

For partial support, SK acknowledges the IoE-IISc fellowship program.

-
- [1] R. Aaij *et al.* [LHCb Collaboration], Phys. Rev. Lett. **113**, 151601 (2014) [[arXiv:1406.6482](#) [hep-ex]].
 - [2] G. Hiller and F. Kruger, Phys. Rev. D **69**, 074020 (2004) [[hep-ph/0310219](#)].
 - [3] M. Bordone, G. Isidori and A. Pattori, Eur. Phys. J. C **76**, no. 8, 440 (2016) [[arXiv:1605.07633](#) [hep-ph]].
 - [4] C. Bouchard *et al.* [HPQCD Collaboration], Phys. Rev. Lett. **111**, no. 16, 162002 (2013) Erratum: [Phys. Rev. Lett. **112**, no. 14, 149902 (2014)] [[arXiv:1306.0434](#) [hep-ph]].
 - [5] R. Aaij *et al.* [LHCb], Phys. Rev. Lett. **122** (2019) no.19, 191801 [[arXiv:1903.09252](#) [hep-ex]].
 - [6] R. Aaij *et al.* [LHCb], JHEP **08** (2017), 055 [[arXiv:1705.05802](#) [hep-ex]].
 - [7] A. Abdesselam *et al.* [Belle], [[arXiv:1904.02440](#) [hep-ex]].
 - [8] R. Aaij *et al.* [LHCb Collaboration], Phys. Rev. Lett. **111**, 191801 (2013) [[arXiv:1308.1707](#) [hep-ex]].
 - [9] R. Aaij *et al.* [LHCb Collaboration], JHEP **1602**, 104 (2016) [[arXiv:1512.04442](#) [hep-ex]].
 - [10] R. Aaij *et al.* [LHCb], Phys. Rev. Lett. **125** (2020) no.1, 011802 [[arXiv:2003.04831](#) [hep-ex]].
 - [11] R. Aaij *et al.* [LHCb Collaboration], JHEP **1509**, 179 (2015) [[arXiv:1506.08777](#) [hep-ex]].
 - [12] M. Algueró, B. Capdevila, A. Crivellin, S. Descotes-Genon, P. Masjuan, J. Matias and J. Virto, Eur. Phys. J. C **79** (2019) no.8, 714 [[arXiv:1903.09578](#) [hep-ph]].
 - [13] A. K. Alok, A. Dighe, S. Gangal and D. Kumar, JHEP **1906**, 089 (2019) [[arXiv:1903.09617](#) [hep-ph]].
 - [14] M. Ciuchini, A. M. Coutinho, M. Fedele, E. Franco, A. Paul, L. Silvestrini and M. Valli, Eur. Phys. J. C **79** (2019) no.8, 719 [[arXiv:1903.09632](#) [hep-ph]].
 - [15] G. D'Amico, M. Nardecchia, P. Panci, F. Sannino, A. Strumia, R. Torre and A. Urbano, JHEP **1709**, 010 (2017) [[arXiv:1704.05438](#) [hep-ph]].
 - [16] J. Aebischer, W. Altmannshofer, D. Guadagnoli, M. Reboud, P. Stangl and D. M. Straub, Eur. Phys. J. C **80** (2020) no.3, 252 [[arXiv:1903.10434](#) [hep-ph]].
 - [17] K. Kowalska, D. Kumar and E. M. Sessolo, Eur. Phys. J. C **79**, no. 10, 840 (2019) [[arXiv:1903.10932](#) [hep-ph]].
 - [18] A. Arbey, T. Hurth, F. Mahmoudi, D. M. Santos and S. Neshatpour, Phys. Rev. D **100**, no. 1, 015045 (2019) [[arXiv:1904.08399](#) [hep-ph]].

- [19] D. Kumar, J. Saini, S. Gangal and S. B. Das, Phys. Rev. D **97** (2018) no.3, 035007 [[arXiv:1711.01989](#) [hep-ph]].
- [20] S. Kumbhakar and J. Saini, Eur. Phys. J. C **79** (2019) no.5, 394 [[arXiv:1807.04055](#) [hep-ph]].
- [21] A. K. Alok, S. Kumbhakar and S. Uma Sankar, [[arXiv:2001.04395](#) [hep-ph]].
- [22] F. Munir Bhutta, Z. R. Huang, C. D. Lü, M. A. Paracha and W. Wang, [[arXiv:2009.03588](#) [hep-ph]].
- [23] J. Kumar and D. London, Phys. Rev. D **99** (2019) no.7, 073008 [[arXiv:1901.04516](#) [hep-ph]].
- [24] A. Datta, J. Kumar and D. London, Phys. Lett. B **797** (2019) 134858 [[arXiv:1903.10086](#) [hep-ph]].
- [25] M. Ciuchini, M. Fedele, E. Franco, S. Mishima, A. Paul, L. Silvestrini and M. Valli, JHEP **06**, 116 (2016) [[arXiv:1512.07157](#) [hep-ph]].
- [26] T. Hurth, F. Mahmoudi and S. Neshatpour, Nucl. Phys. B **909**, 737-777 (2016) [[arXiv:1603.00865](#) [hep-ph]].
- [27] V. G. Chobanova, T. Hurth, F. Mahmoudi, D. Martinez Santos and S. Neshatpour, JHEP **07**, 025 (2017) [[arXiv:1702.02234](#) [hep-ph]].
- [28] T. Hurth, F. Mahmoudi and S. Neshatpour, [[arXiv:2006.04213](#) [hep-ph]].
- [29] G. Hiller and M. Schmaltz, Phys. Rev. D **90** (2014), 054014 [[arXiv:1408.1627](#) [hep-ph]].
- [30] D. Bardhan, P. Byakti and D. Ghosh, Phys. Lett. B **773**, 505-512 (2017) [[arXiv:1705.09305](#) [hep-ph]].
- [31] R. Aaij *et al.* [LHCb], Phys. Rev. Lett. **124** (2020) no.21, 211802 [[arXiv:2003.03999](#) [hep-ex]].
- [32] R. Aaij *et al.* [LHCb], JHEP **05** (2013), 159 [[arXiv:1304.3035](#) [hep-ex]].
- [33] R. Aaij *et al.* [LHCb], JHEP **04** (2015), 064 [[arXiv:1501.03038](#) [hep-ex]].
- [34] J. P. Lees *et al.* [BaBar], Phys. Rev. Lett. **112** (2014), 211802 [[arXiv:1312.5364](#) [hep-ex]].
- [35] S. Wehle *et al.* [Belle], Phys. Rev. Lett. **118** (2017) no.11, 111801 [[arXiv:1612.05014](#) [hep-ex]].
- [36] D. M. Straub, [[arXiv:1810.08132](#) [hep-ph]].
- [37] A. Bharucha, D. M. Straub and R. Zwicky, JHEP **08** (2016), 098 [[arXiv:1503.05534](#) [hep-ph]].
- [38] N. Gubernari, A. Kokulu and D. van Dyk, JHEP **01** (2019), 150 [[arXiv:1811.00983](#) [hep-ph]].
- [39] A. Khodjamirian, T. Mannel, A. A. Pivovarov and Y. M. Wang, JHEP **09** (2010), 089 [[arXiv:1006.4945](#) [hep-ph]].
- [40] F. James and M. Roos, Comput. Phys. Commun. **10** (1975), 343-367
- [41] F. James, CERN-D-506.
- [42] C. Bobeth, G. Hiller and G. Piranishvili, JHEP **07** (2008), 106 [[arXiv:0805.2525](#) [hep-ph]].
- [43] W. Altmannshofer, P. Ball, A. Bharucha, A. J. Buras, D. M. Straub and M. Wick, JHEP **01** (2009), 019 [[arXiv:0811.1214](#) [hep-ph]].
- [44] S. Descotes-Genon, J. Matias, M. Ramon and J. Virto, JHEP **01** (2013), 048 [[arXiv:1207.2753](#) [hep-ph]].